


Chemical Insights into the Design and Development of Face-Centered Cubic Ruthenium Catalysts for Fischer–Tropsch Synthesis

Wei-Zhen Li,^{†,⊗} Jin-Xun Liu,^{‡,⊗} Jun Gu,^{†,⊗} Wu Zhou,^{§,||} Si-Yu Yao,[†] Rui Si,[#] Yu Guo,[†] Hai-Yan Su,[⊥] Chun-Hua Yan,[†] Wei-Xue Li,^{*,‡,⊗} Ya-Wen Zhang,^{*,†} and Ding Ma^{*,†} 

[†]Beijing National Laboratory for Molecular Sciences (BNLMS), College of Chemistry and Molecular Engineering, Peking University, Beijing 100871, China

[‡]Department of Chemical Physics, College of Chemistry and Materials Science, iChEM, CAS Center for Excellence in Nanoscience, Hefei National Laboratory for Physical Sciences at the Microscale, University of Science and Technology of China, Hefei 230026, China

[§]School of Physical Sciences, CAS Key Laboratory of Vacuum Sciences, University of Chinese Academy of Sciences, Beijing 100049, China

^{||}Materials Science and Technology Division, Oak Ridge National Laboratory, Oak Ridge, Tennessee 37831, United States

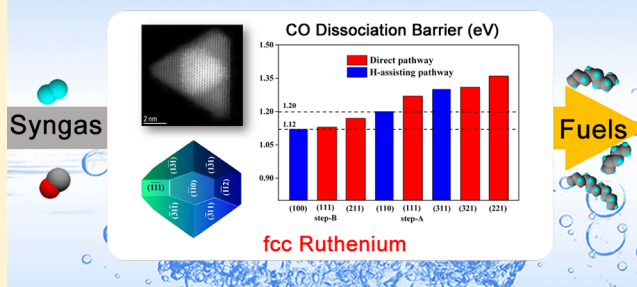
[⊥]State Key Laboratory of Catalysis, State Key Laboratory of Molecular Reaction Dynamics, Dalian Institute of Chemical Physics, Chinese Academy of Sciences, Dalian 116023, China

[#]Shanghai Synchrotron Radiation Facility, Shanghai Institute of Applied Physics, Chinese Academy of Sciences, Shanghai 201204, China

Supporting Information

ABSTRACT: Ruthenium is a promising low-temperature catalyst for Fischer–Tropsch synthesis (FTS). However, its scarcity and modest specific activity limit its widespread industrialization. We demonstrate here a strategy for tuning the crystal phase of catalysts to expose denser and active sites for a higher mass-specific activity. Density functional theory calculations show that upon CO dissociation there are a number of open facets with modest barrier available on the face-centered cubic (fcc) Ru but only a few step edges with a lower barrier on conventional hexagonal-closest packed (hcp) Ru. Guided by theoretical calculations, water-dispersible fcc Ru catalysts containing abundant open facets were synthesized and showed an unprecedented mass-specific activity in the aqueous-phase FTS, $37.8 \text{ mol}_{\text{CO}} \cdot \text{mol}_{\text{Ru}}^{-1} \cdot \text{h}^{-1}$ at 433 K. The mass-specific activity of the fcc Ru catalysts with an average size of 6.8 nm is about three times larger than the previous best hcp catalyst with a smaller size of 1.9 nm and a higher specific surface area. The origin of the higher mass-specific activity of the fcc Ru catalysts is identified experimentally from the 2 orders of magnitude higher density of the active sites, despite its slightly higher apparent barrier. Experimental results are in excellent agreement with prediction of theory. The great influence of the crystal phases on site distribution and their intrinsic activities revealed here provides a rationale design of catalysts for higher mass-specific activity without decrease of the particle size.

Aqueous Fischer-Tropsch Synthesis



INTRODUCTION

To develop efficient heterogeneous catalysts with higher mass specific activity and stability is currently challenging and demanding due to the limited resources available for energy conversion, chemical production, and environment protection. Specifically, it is highly desirable to develop efficient Fischer–Tropsch synthesis (FTS) catalysts that are used for production of liquid fuels and chemicals from coal, shale gas, and biomass that can work at low reaction temperature. Compared to the cobalt- and iron-based FTS processes typically working at 493–623 K,^{1–17} ruthenium (Ru) catalysts are promising because they are active at lower temperatures.^{18–20} However, its scarcity and modest mass-specific activity require more investigation to

increase mass-specific activity and stability prerequisite for its widespread industrialization.

To increase the mass-specific activity, the most used strategy is to reduce the particle size and thus to expose more surface sites.^{21–23} This works well for structure-insensitive reactions with an increased tendency toward sintering and/or disintegration of supported particles.^{24–30} For some of the structure-sensitive reactions, the activity in terms of, for instance, turnover frequency (TOF) might even decrease with a reduction of the particle size.^{8,21,22,31,32} Accordingly, identification of the

Received: October 4, 2016

Published: January 18, 2017

active sites and its structural sensitivity is crucial. The edge sites of metal particles are usually highly active due to their lower coordination number, though the corresponding site density is low.^{33–35} Shape control to expose specific facets with desired activity and higher site density is a promising strategy; however, the performance of catalysts is often degraded by the strong protecting agents used to expose specific facets of catalysts.^{36–40} Therefore, the synthesis of catalysts with abundant active sites and free of protecting agents yet stable is vital for catalyst design with high specific activity.⁴¹

There is growing interest in the effect of the exposed crystal phases of the metal particles on catalytic activity and selectivity.^{42–56} For cobalt-catalyzed FTS, it was found by Ducreux et al.^{42,43} and confirmed by many others^{44–47} that the hcp phase is more active than the face-centered-cubic (fcc) phase. Based on density functional theory (DFT) calculations and kinetics analysis, we found that CO dissociation on hcp Co has a lower CO dissociation barrier compared with fcc Co and dissociates directly for the previous one but is assisted by hydrogen for the latter one.⁴⁸ The origin of higher catalytic activity on hcp Co came from the formation of abundant 4-fold sites favorable for stabilizing dissociation products. When the cobalt was carburized to the carbide phase, which is inactive for FTS, we found that the formation of the Co metal and carbide interfaces dramatically increases the selectivity of high alcohol.⁵⁵ Recent experiments further showed that controlling the morphology of cobalt carbide can even produce the lower olefin highly selectively.⁵⁶

The formation of a mixed phase of fcc and hcp Ru was first observed by Somorjai and co-workers⁵⁷ in Ru catalyst for CO oxidation. A pure fcc Ru phase was later synthesized by Kitagawa et al.⁵⁸ Different from Co catalysts, fcc Ru was more active toward CO oxidation than that of hcp Ru when the size was above 3 nm. It was proposed that the higher activity of fcc Ru came from the presence of abundant (111) facets, which could be easily oxidized to more active RuO₂ (110). We also synthesized fcc Ru but using fcc Pt as core and found that the synthesized core–shell Pt@Ru catalysts composing a number of (111) facets is more active for hydrogen evolution reaction than that of hcp Ru.⁵⁹ Higher activity of fcc Ru compared to hcp Ru was further observed in other reactions, such as conversion of ammonia–borane,^{60–62} oxygen evolution reaction,⁶³ hydrogenation reaction,⁶⁴ and N₂ activation.⁶⁵ Whether fcc Ru have higher activity than that of hcp Ru toward FTS remains an open question.

We report here a joint theoretical and experimental study on fcc and hcp Ru-catalyzed FTS. To guide the catalyst synthesis, we first used CO dissociation to probe the influence of fcc and hcp Ru via DFT calculations. It was found that there are a number of open facets with modest barriers available on fcc Ru but only a few step edges with a lower barrier on hcp Ru. On the basis of theoretical calculations, water-dispersible fcc Pt@Ru core–shell nanocrystal catalysts with high density of the active sites (open facets) were synthesized. The fcc NCs catalyst synthesized shows extraordinary specific activity in the aqueous-phase FTS process in a low temperature range of 393–433 K. At 433 K, the activity is as high as 37.8 mol_{CO}·mol_{Ru}⁻¹·h⁻¹, which is by far the most active FTS catalyst working at low temperature (<473 K). The origin of the high activity of fcc Ru compared with hcp Ru is identified to result from the at least 2 orders of magnitude higher density of active sites on fcc NCs catalysts, as predicted by theoretical calculations. Importantly, an increase of the site density allows

the synthesis of catalysts for a higher specific activity without decrease of the particle size, a fact of that improves the stability of catalysts as well.

RESULTS AND DISCUSSION

DFT Calculations. Hcp and fcc Ru have different crystal structures and can expose various sites with distinct intrinsic activity and population. To examine the overall feature of hcp and fcc Ru rather than to study only a few representative step edges/facets, we started first from the fcc and hcp Ru bulk morphologies, which indicate the potential facets exposed and the corresponding ratio. On the basis of the principle of Wulff construction and surface energies of a number of surfaces from DFT calculations (Table S1), the morphology of bulk fcc and hcp Ru was optimized (Figure S1). Indeed, fcc and hcp Ru bulks exhibit very different morphologies: fcc Ru is octahedron-like populated mainly by close-packed (111) facets, and hcp Ru is a dihedral-like shape populated mainly by open facets, respectively. To probe the influence of the Ru crystal phase (hcp vs fcc) on the FTS reactivity, CO dissociation, which is a crucial step for FTS, was calculated. We considered 18 surface structures, including facets exposed in optimized morphologies of bulk metals, and a few low index facets including (111) and (0001) steps (both A type and B type), which might be important for small particles. Two possible dissociation pathways, namely, direct dissociation (CO → C + O) and H-assisting dissociation (CO + H → CHO → CH + O), at low coverages of 0.25 ML were explored. The corresponding energetics, kinetics barriers, configuration for reactants, intermediates, and transition states are reported in Table S2 and Figure S2.

The calculated CO dissociation barriers, E_{diss} , vary from 0.94 to 2.37 eV for hcp Ru and 1.13 to 2.28 eV for fcc Ru, respectively. The large variation of CO dissociation barriers in magnitude of 1.43 eV (hcp) and 1.15 eV (fcc) suggests that CO dissociations are highly structure sensitive on both Ru phases. This is in good agreement with the result of diatomic molecules dissociation on transition-metal surfaces.^{21,35,66–68} Considering typical aqueous-phase FTS reaction conditions (393–443 K), an increase of the dissociation barrier by 0.1 eV means a decrease of the corresponding rate constant by more than 1 order of magnitude. As a result, we focus below the structures with CO dissociation barrier falling in the window of 0.94–1.39 eV only, which contains 14 of 18 different surface structures (Figure 1).

From Figure 1, it is observed that hcp (0001) step B has the lowest CO dissociation barrier E_{diss} of 0.94 eV via direct dissociation, among all structures considered. The low barrier comes from the presence of favorable B5-sites,^{21,22,35} as shown in Figure 2A. This implies that hcp Ru might have potentially higher intrinsic activity than fcc Ru. However, the site density of the step edge is low and might even disappear in small particles.^{21,22,35} For structures with a CO dissociation barrier in range of [1.12 eV, 1.20 eV], there is only one facet available from hcp Ru, (11 $\bar{2}$ 1), where CO dissociates directly with a barrier of 1.13 eV. In contrast, for fcc Ru, there is one step edge (111) step B, and three facets including (100), (211), and (110) available. The corresponding CO dissociation barriers are 1.13, 1.12, 1.17, and 1.20 eV, respectively. Depending on the facet, CO dissociates directly or assisting by hydrogen, as indicated in Figure 1. Again, the modest barriers for these facets originate from the presence of B5-type sites (Figure 2B–D). More fcc facets than those of hcp Ru in the CO dissociation

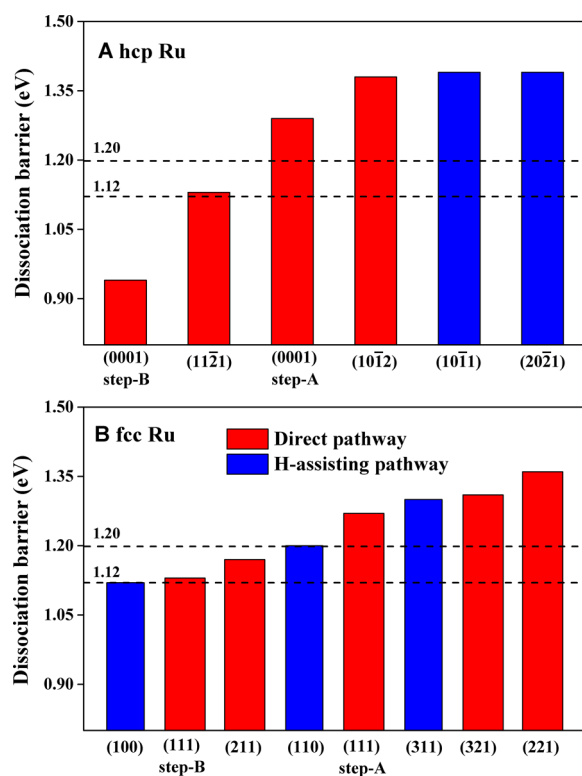


Figure 1. Calculated CO dissociation barriers on various hcp (A) and fcc (B) Ru facets and step edges. Only the favorable reaction pathways are indicated: red for direct dissociation and blue for H-assisting dissociation. Two horizontal dashed lines separate the structures considered in three dissociation barrier windows, less than 1.12 eV, [1.12 eV, 1.20 eV], and larger than 1.20 eV, respectively.

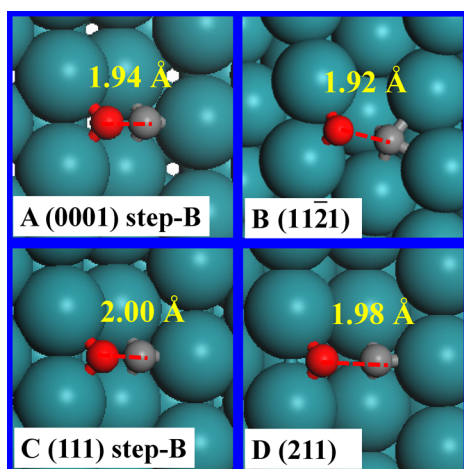


Figure 2. Schematic transition states (TSs) for CO direct dissociation on hcp (0001) B step (A) and (1121) facet (B) and fcc (111) step B (C), (211) facet (D). Green (large), red, gray, and white (small) balls are ruthenium, oxygen, carbon, and hydrogen atoms, respectively. The distance between C and O atoms at the TS are indicated.

barrier of [1.12 eV, 1.20 eV] indicate that there are denser active sites available on fcc Ru.

For hcp Ru structures with CO dissociation barriers higher than 1.20 eV (Figure 1), there are four structures available, i.e., (0001) step A, (1121), (1011), and (2021) with values of 1.29, 1.38, 1.39, and 1.39 eV, respectively, while for fcc Ru there are also four structures available, i.e., (111) step A, (311), (321),

and (221) with E_{diss} of 1.27, 1.30, 1.31, and 1.36 eV, respectively. Compared to the above structures in [1.12 eV, 1.20 eV], the corresponding rate constants of CO dissociation would decrease by 1 and/or 2 orders of magnitude further. Importantly, since both fcc and hcp Ru have similar amounts of facets/step edges in this window, their contribution to the overall activity of fcc and hcp Ru would be similar.

The above calculations indicate that hcp Ru (0001) step-B sites have a lower barrier for CO dissociation, but its site density is rather low. This would limit the specific activity of the hcp Ru catalyst. On other hand, though fcc Ru has facets with slightly higher barriers, the corresponding sites is more abundant. This implies that fcc Ru catalyst might have an overall higher mass-specific activity, as indeed seen in following experiment.

We note that the trend behavior between the hcp and fcc phase is dependent on the transition metals. For instance, on cobalt catalysts, hcp Co not only has lower barriers for CO dissociation but also has more active facets than that of fcc Co.⁴⁸ The difference between Ru and Co comes mainly from, in addition to the electronic effect (composition), the geometrical effect. Namely, the Ru lattice constant is about 9% larger than that of Co, a fact of that change the corresponding transition states, as found similar in our previous work.⁶⁹

Synthesis of fcc Ru Nanocrystals. Fcc Ru nanocrystals (noted as fcc NCs) have been reported recently by several groups including us.^{58–65} It was proposed that the presence of abundant (111) facets was essential for the observed superior activity,⁵⁸ whereas our calculations above indicate that, for CO dissociation, abundant open facets are desired. Moreover, for aqueous FTS, it is also crucial to synthesize water-stable and dispersible catalysts free from strong protecting agents.

Herein, we synthesized fcc Pt@Ru core–shell nanocrystals (Pt/Ru = 1:9 in mole ratio) with a hydrothermal method. K_2PtCl_4 and RuCl_3 were used as metal precursors. Formaldehyde was introduced as the reductant and polyvinylpyrrolidone (PVP) as a weak polymeric stabilizer to make the nanocrystals dispersible in aqueous solution. During the hydrothermal reaction at 433 K, fcc Pt cores formed, followed by the epitaxial growth of fcc Ru shells. The obtained NCs show an average size of 6.8 ± 1.5 nm (Figure 3A, noted as fcc NCs (6.8 nm)). The Pt/Ru molar ratio of the NCs obtained from EDS (Figure 3C) and inductively coupled plasma-atomic emission spectrometry (ICP-AES) is identical with the feeding ratio of the two metals (Table S3), suggesting the complete reduction of both precursors.

A representative scanning transmission electron microscopy (STEM) image in annular dark field (ADF) Z-contrast mode shows that almost all NCs contain a bright Pt core (2–4 nm) fully wrapped by a less bright Ru shell. This is further supported by the elemental mapping via electron energy-loss spectroscopy (EELS) imaging (Figure 3D–G). Only one set of diffraction patterns, corresponding to the [110] zone axis of the fcc phase, is observed in the fast Fourier transform (FFT) of the image of the entire particle in Figure 3F, revealing the fcc nature of this particle and overgrowth of the Ru shell on the Pt core.

The fcc NCs synthesized are metallic in nature according to normalized X-ray absorption near-edge structure experiments (Figure S4), and the core–shell nature of the particles was further confirmed by the extended X-ray absorption fine structure (EXAFS) spectrum. For the Pt L3 edge, the sum of the first shell coordination number of $N_{\text{Pt–Pt}}$ and $N_{\text{Pt–Ru}}$ is 11.6,

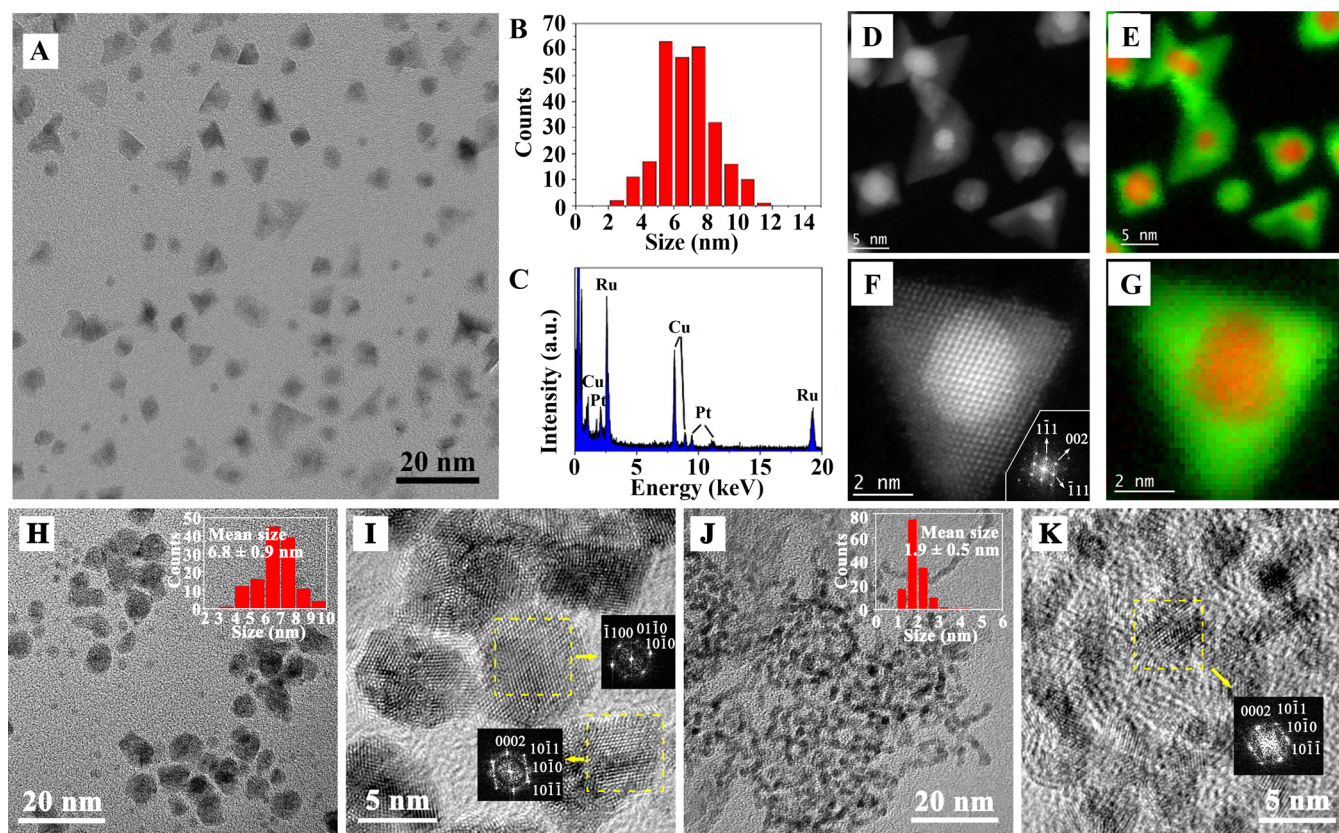


Figure 3. (A–G) Electron microscopic characterization of fcc NCs: (A) TEM image; (B) size distribution histogram (counted number of particles, 270); (C) EDS spectrum; (D, F) STEM ADF images; and (E, G) corresponding EELS mapping images (red for Pt and green for Ru). The inset of panel F shows the FFT pattern of the STEM ADF image. (H–K) Electron microscopic characterization of hcp NCs: (H) TEM and (I) HRTEM of 6.8 nm hcp NCs. (J) TEM and (K) HRTEM of 1.9 nm hcp NCs. The insets of panels H and J show the size distribution histogram of NCs in the corresponding TEM images (counted number of particles, 170, for each sample). The insets of panels I and K show the FFT patterns of the regions surrounded by yellow dashed lines.

while $N_{\text{Ru-Ru}}$ in the Ru K edge is 9.1. Moreover, $N_{\text{Ru-Pt}}$ in the Ru K edge is undetectable (Figure 4B and Table 1). This

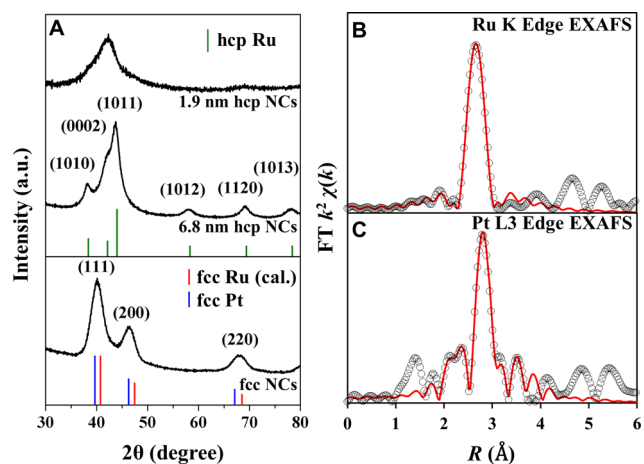


Figure 4. (A) XRD patterns of fcc NCs (bottom), 6.8 nm hcp NCs (middle) and 1.9 nm hcp NCs (top). Red, blue, and green vertical lines indicate the standard diffraction peaks of fcc Ru (calculated pattern, space group: $Fm\bar{3}m$, no. 88-2333), fcc Pt (space group: $Fm\bar{3}m$, no. 04-0802), and hcp Ru (space group: $P63/mmc$, no. 06-0663), respectively. (B) Ru K edge and (C) Pt L3 edge EXAFS spectra (black dots) of fcc NCs with the fitting curves (red lines). The specific contribution for each shell is shown in Figures S5–S7.

Table 1. Coordination Numbers Obtained from EXAFS Fitting for fcc NCs, Pt Foil, and Ru Foil^a

sample	coordination		CN
Pt foil	Pt L3	Pt–Pt	12
Ru foil	Ru K	Ru–Ru	6 + 6
fcc NCs	Pt L3	Pt–Pt	9.7 ± 1.3
		Pt–Ru	1.9 ± 0.4
	Ru K	Ru–Ru	9.1 ± 0.6
		Ru–Pt	not detected

^afor details, see Figures S5–S7 and Table S4.

suggests that Pt atoms are in saturated coordination with all Pt atoms either adjacent to Pt atoms or Ru atoms, while part of the Ru atoms are unsaturated. In other words, Pt and Ru are in a kind of core (Pt) shell (Ru) structure.⁷⁰

Compared with fcc Ru nanocrystals in previous reports, the samples in this work show wider distributions in size and expose more open facets which will be discussed in detail later. According to the DFT results above, the activation energy of CO dissociation is relatively low on these open facets of fcc Ru. In the previous reports, capping agents with stabilizing effects on certain facets were introduced to improve the morphology uniformity of fcc Ru nanocrystals. For instance, oxalate ions, selectively stabilizing {111} facets of fcc Ru,⁵⁹ and fcc Pt–Pd alloy,^{71,72} were used in the synthesis of fcc Pt@Ru nanotetrahedrons surrounded by {111} facets. In the present work,

no such capping agent is added, and therefore, fcc Pt@Ru nanocrystals expose fewer {111} facets and more open facets are obtained, as revealed by the structure analysis based on the STEM-ADF method in the latter part of this paper.

As a control sample, we also synthesized hcp NCs at similar size of 6.8 ± 0.9 nm (Figure 3H, termed as hcp NCs (6.8 nm)). These Ru NCs are hcp particles with a polycrystalline feature, as shown by the high-resolution TEM (HRTEM) image (Figure 3I). A hcp domain from the $[11\bar{2}0]$ zone axis is shown in the lower right part of Figure 3I, which exposes both {0001} facets and open facets of hcp phase. Another reference sample (termed as hcp NCs (1.9 nm)) is hcp Ru nanospheres with an average diameter of 1.9 ± 0.5 nm (Figure 3J). These nanospheres coalesce to form networks of interconnecting nanoparticles. A hcp domain projected from the $[11\bar{2}0]$ zone axis is highlighted in the HRTEM image (Figure 3K). In previous records, this sample shows the highest TOF in aqueous-phase FTS.¹⁸

A typical X-ray diffraction (XRD) pattern of the as-obtained fcc NCs shows characteristic peaks at 40.3° , 46.6° , 68.2° (2θ), corresponding to the (111), (200), and (220) diffractions of fcc phase (lower part of Figure 4A). Rietveld refinement (Figure S3A, $R_{wp} = 0.0235$, $R_{exp} = 0.0229$, GOF = 1.03) further confirms the fcc structure of Pt cores ($a = 3.963$ Å) and Ru shells ($a = 3.893$ Å). The Ru–Ru distance in fcc Ru shells is slightly smaller than the Pt–Pt distance in fcc Pt cores, in accordance with the EXAFS fitting result (Table S4). The molar ratio of fcc Pt phase to fcc Ru phase is 10.2:89.8, quite close to the feeding ratio of two precursors. XRD pattern of hcp phase is observed on the 6.8 nm hcp NCs (middle part of Figure 4A). The refinement of the XRD profile (Figure S3C, $R_{wp} = 0.0303$, $R_{exp} = 0.0278$, GOF = 1.09) indicates lattice parameters of $a = b = 2.710$ Å and $c = 4.298$ Å, identical to those in the PDF card (No. 06-0663). The excellent agreement with the DFT calculation of $a = b = 2.728$ Å and $c = 4.297$ Å for bulk hcp Ru tells that 6.8 nm hcp NCs already have good crystalline bulk structures, whereas for the 1.9 nm hcp NCs, because of its ultrasmall size, the diffraction peaks around 40 – 43° widen seriously, merging into a broad peak in the XRD profile (upper part of Figure 4A).

FTS Performance. Although FTS is favored at low temperature, the conventional gas-phase Ru-, Co-, and Fe-based FTS catalysts (Table S5) normally have relatively low reactivity. Normally, gas-phase FTS is operating within a temperature range of 493–673 K.^{1–5} In 2007, it was reported that FTS could be operated in the aqueous phase as well, even at the low temperature of 423 K, and hcp Ru nanoparticle catalysts are very active in aqueous-phase FTS, reaching a record-high activity of $6.9 \text{ mol}_{\text{CO}} \cdot \text{mol}_{\text{Ru}}^{-1} \cdot \text{h}^{-1}$ at that low temperature.¹⁸

In order to know whether the synthesized aqueous-phase water-soluble fcc NC catalyst has an improved catalytic performance in FTS and could surpass the previously best catalyst, we evaluated the above catalysts in aqueous phase at a relatively low temperature of 403 to 433 K (3.0 MPa syngas, $\text{H}_2/\text{CO} = 2:1$, Figure 5A and Figure S10A). We used mass-specific activity (r_{ms}) as a measure as it represents the mass-based potential of the catalysts. A higher mass-specific activity means that it is able to use less amount of expensive catalyst, which is critical for the industrial application of a new catalyst.

At 413 K, the mass-specific activity, r_{ms} , of hcp NCs (1.9 nm), which are the most active aqueous phase FTS catalysts reported so far, was $3.7 \text{ mol}_{\text{CO}} \cdot \text{mol}_{\text{Ru}}^{-1} \cdot \text{h}^{-1}$.¹⁸ For 6.8 nm hcp

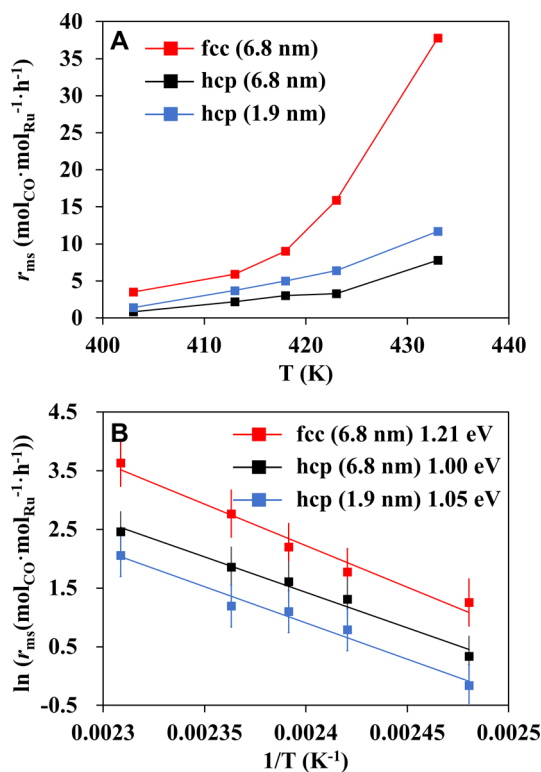


Figure 5. Reaction performance of Ru catalysts. (A) Activity of fcc NCs (6.8 nm), hcp NCs (6.8 and 1.9 nm) at 413 and 433 K. (B) The Arrhenius plot and the extracted apparent FTS barriers are indicated. The reaction was conducted at 3.0 MPa syngas ($\text{CO}/\text{H}_2 = 1:2$ mol ratio), 0.2 mmol catalyst, 800 rpm stirring.

NCs, it dropped to $2.2 \text{ mol}_{\text{CO}} \cdot \text{mol}_{\text{Ru}}^{-1} \cdot \text{h}^{-1}$, due to the lower specific surface area, whereas for fcc NCs catalysts, the r_{ms} increased drastically to $5.9 \text{ mol}_{\text{CO}} \cdot \text{mol}_{\text{Ru}}^{-1} \cdot \text{h}^{-1}$ (Figure 5A). At 433 K, the r_{ms} of the three catalysts increased rapidly to 37.8, 7.8, and $11.7 \text{ mol}_{\text{CO}} \cdot \text{mol}_{\text{Ru}}^{-1} \cdot \text{h}^{-1}$ for fcc NCs and hcp NCs (6.8 and 1.9 nm), respectively. Moreover, it can be found that the superior performance of fcc NCs over hcp NCs is enlarged at higher temperature. Specifically, the r_{ms} of fcc NCs becomes about five times higher than the hcp NCs with same particle size and at least three times higher than 1.9 nm hcp NCs. The activity of fcc NCs is also significantly higher than any reported aqueous phase FTS catalysts at same temperature.^{18,73–77}

The TOF of fcc and hcp NCs were calculated on the basis of the moles of CO per moles of surface Ru atom converted per hour, assuming all surface Ru atoms exposed are equally active and the particles are spherical (Figure S9). At 433 K, the TOF of 6.8 nm fcc NCs is as high as $197 \text{ mol}_{\text{CO}} \cdot \text{mol}_{\text{surf-Ru}}^{-1} \cdot \text{h}^{-1}$, in sharp contrast to $17 \text{ mol}_{\text{CO}} \cdot \text{mol}_{\text{surf-Ru}}^{-1} \cdot \text{h}^{-1}$ of 1.9 nm hcp NCs (the most active catalyst reported previously). Namely, the TOF of fcc NCs is more than 1 order of magnitude higher than the previous best catalyst.

The product distributions of the reaction at 433 K are shown in Figure 6. The chain-length distribution of the hydrocarbon products on fcc NCs follows the Anderson–Schulz–Flory statistics (Figure 6A) with a growth factor (α) of hydrocarbon products of 0.81 (C_{1-19}), whereas those of hcp NCs (1.9 and 6.8 nm) are 0.83 and 0.77, respectively. Significantly, the selectivity toward the most desired product C_{5+} of fcc NCs catalyst was as high as 81.3% (Figures 6B). Small amounts of alcohols (3.8%) and aldehydes (2.6%) were also generated. On

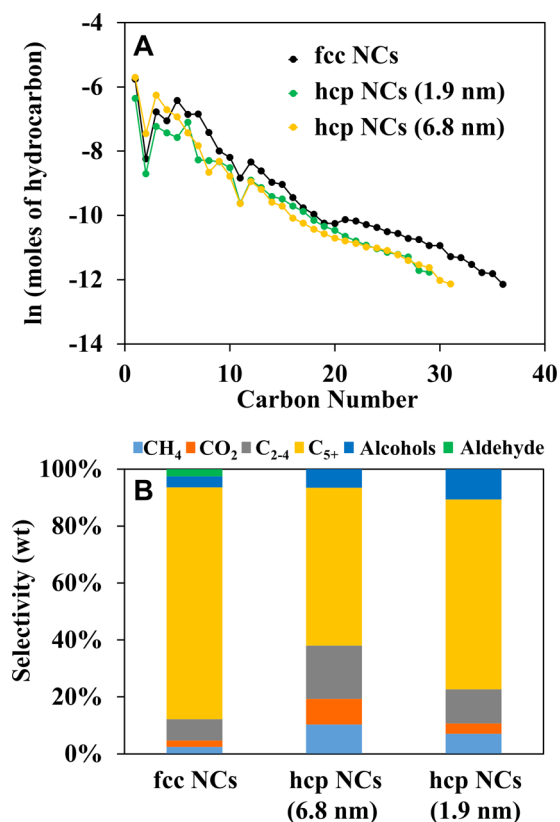


Figure 6. (A) Anderson–Schulz–Flory distribution of hydrocarbon products for fcc NCs and hcp NCs. (B) Product distribution at 433 K (for more details, see Figure S10).

the other hand, the selectivity toward undesirable CO₂ and CH₄ were only 7.5% and 2.5%, respectively, showing that this catalyst is indeed excellent in terms of carbon source utilization efficiency. In comparison, the selectivity toward C₅₊ product was only 55.4–66.7% for hcp NCs, while the selectivities toward CO₂ and CH₄ were 3.7–9.0% and 7.0–10.3%, respectively. The lower selectivity of CH₄ on fcc Ru as compared to hcp Ru can be attributed to the stronger adsorption of C atom on fcc Ru (Table S2-1, $E_C = -8.10$ eV/fcc (211) vs -7.59 eV/hcp (11 $\bar{2}$ 1)), as found in previous theoretical calculations where the stronger adsorption of C atom leads to a lower CH₄ selectivity.^{78,79}

To reveal the origin of the higher activity r_{ms} of fcc NCs than that of hcp NCs, we first performed the FTS experiment at different temperatures (Figure 5A), from which the apparent FTS barriers E_{app} can be extracted based on the Arrhenius equation. Significantly, the extracted barriers E_{app} for hcp NCs are 1.00 eV for 6.8 nm catalyst and 1.05 eV for 1.9 nm catalyst, showing that the reaction barrier is nearly independent of the size of hcp NCs. For fcc NCs (6.8 nm), surprisingly, the corresponding E_{app} is larger with value of 1.21 eV, in contrast to its higher specific activity. Nevertheless, the measured trend of E_{app} between 6.8 nm fcc and hcp NCs (1.21 eV vs 1.00 eV) agrees well with the trend of the calculated least CO dissociation barrier between fcc and hcp Ru (1.12 eV vs 0.93 eV). The qualitative and even the quantitative agreement (with an offset of ~ 0.08 eV in average) between experiment and theory substantiates well the theoretical prediction on the different intrinsic activity of the surface sites on fcc and hcp Ru catalysts. Moreover, this agreement also highlights the importance of CO dissociation on the overall activity of FTS.

We now turn to see the influence of the hcp and fcc phases on vibrational factor A_{vib} involved in rate constant. For simplicity, we resort to examining direct CO dissociation on typical step edges and facets, including hcp (0001) and fcc (111) step B and hcp (11 $\bar{2}$ 1) and fcc (211) by DFT calculations. A_{vib} can be calculated via the corresponding partition functions of CO dissociation at the transition state and adsorption state Q_{TS} and Q_{CO} based on the transition state theory. The A_{vib} for hcp (0001) and fcc (111) step B are computed to be similar ($1.3 \times 10^{11} \text{ s}^{-1}$ vs $2.0 \times 10^{11} \text{ s}^{-1}$), whereas for open facets, the calculated A_{vib} of hcp (11 $\bar{2}$ 1) is about five times larger than that of fcc (211) ($3.3 \times 10^{12} \text{ s}^{-1}$ vs $6.0 \times 10^{11} \text{ s}^{-1}$). Considering the approximation of the harmonic theory, the present result indicates that influence of the hcp and fcc phases on A_{vib} is small. For simplification, the vibrational factor of the fcc and hcp phases was assumed same at below.

For a given catalyst, the corresponding mass-specific activity is governed in large extent by resultant of an exponential function of the apparent FTS barrier via $\text{Exp}(-E_{app}/k_B T)$, vibrational factor, and the active site density. Based on the measured mass-specific activity r_{ms} , extracted apparent FTS barriers E_{app} and assumption of same vibrational factor of fcc and hcp NCs, the ratio of the site density responsible for the measured FTS activity between the best fcc and hcp NCs can be estimated. The site density on fcc NCs (6.8 nm) is around 2 orders of magnitude higher than that of hcp NCs (1.9 nm) on average. This corroborates well with the theoretical proposal of the denser active sites on fcc Ru.

STEM-ADF imaging was employed to substantiate the presence of denser active sites on fcc NCs. Even though the fcc NCs are not monodispersed and show various projected morphologies in the TEM images (Figure 3A) as they lay along different orientations on the carbon film, the majority of the NCs prefer to having some common structural features. A typical STEM-ADF image is shown in Figure 7A. The

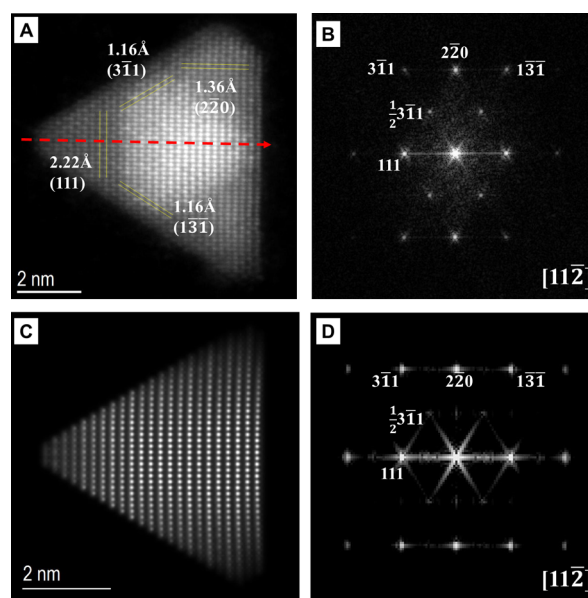


Figure 7. Structural analysis of a representative fcc NCs. Atomic resolution STEM ADF image (A) and corresponding FFT (B) along the fcc [11 $\bar{2}$] zone axis showing quasi-triangular projection and the presence of only one set of diffraction pattern, respectively. (C) Simulated STEM ADF image along the fcc [11 $\bar{2}$] zone axis. (D) FFT of the simulated image.

corresponding fast Fourier transformation (Figure 7B) shows that the three edges of the particle are parallel to one set of $\{111\}$ planes and two sets of $\{311\}$ planes. The ADF image intensity profile (Figure S11), taken across the $\{111\}$ planes, reveals a gradual increase of intensity from the vertex or base of the triangle projection toward the center of the nanoparticle. This is true even just within the Ru shell layers (as seen from the intensity line profile from the Ru EELS map, Figure S12), suggesting that the nanoparticle is not flat. Instead, the thickness along the highlighted trajectory is increasing toward the center of the triangular projection.

Accordingly, a polyhedron model with surfaces composed of $\{111\}$, $\{311\}$, $\{211\}$, and $\{110\}$ facets was constructed and shown in Figure 8 viewed from different angles (animation in

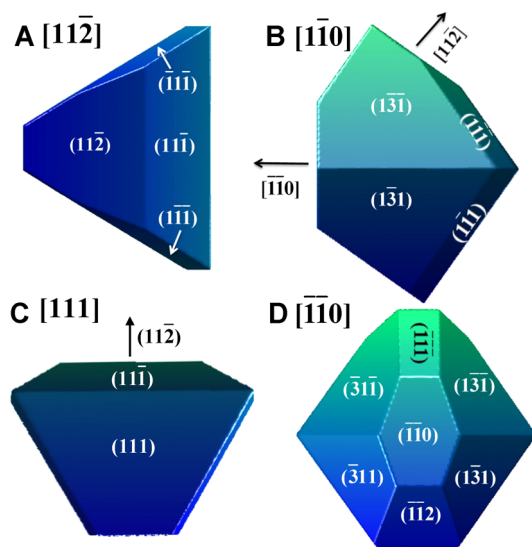


Figure 8. Proposed fcc NCs model viewed along the $[11\bar{2}]$ (A), $[1\bar{1}0]$ (B), $[111]$ (C), and $[\bar{1}\bar{1}0]$ (D) directions, respectively. Exposed facets and normal directions are indicated in parentheses and square brackets.

Figure S13). STEM image simulation (Figure 7C) based on the proposed 3D structure, without the Pt core, can well reproduce the quasi-triangular projection along the $[11\bar{2}]$ direction and the intensity profile. FFT of the simulated STEM image (Figure 7D) shows the presence of the $1/2\{311\}$ super-reflection spots, which are observed in the experimental image of our fcc but not in bulk fcc metals (Figure 7B). Simulation along the $[110]$ zone axis also agrees with the corresponding experimental image (Figure S14). The excellent agreement between simulation and experimental images suggests that the constructed polyhedron captures the overall shape and exposed surface facets of the fcc NCs.

From the constructed polyhedron, the ratio of $\{111\}$, $\{311\}$, $\{211\}$, and $\{110\}$ facets exposed can be derived, and the corresponding values are 40%, 41%, 13%, and 6%. Since the calculated CO dissociation barriers on these low-index open facets (1.30, 1.17 and 1.20 eV for $\{311\}$, $\{211\}$, and $\{110\}$, respectively) are modest, the presence of the dense and active sites on fcc NCs is well substantiated. Moreover, there remains a high ratio of $\{111\}$ facet (40%) exposed, and the amount of (111) B-type step edge with low CO dissociation barrier of 1.13 eV might also contribute to the overall activity. These sites confer the extraordinary specific FTS activity of fcc NCs Ru catalysts.

We note that the fcc NCs exhibit excellent stability during FTS. Recycling experiments at 423 K indicate that r_{ms} decreases only slightly in the third run from 15.0 to 13.9 $\text{mol}_{\text{CO}} \cdot \text{mol}_{\text{Ru}}^{-1} \cdot \text{h}^{-1}$ and then remains almost unchanged during the remaining tests with a value of 12.9–13.9 $\text{mol}_{\text{CO}} \cdot \text{mol}_{\text{Ru}}^{-1} \cdot \text{h}^{-1}$; similar results were found for selectivity (Figure S15). The TEM and XRD results showed that the phase and structure of the fcc NCs remain unchanged after the reaction (Figure S16), and thus, the fcc NCs are inferred to be stable during the FTS reaction.

The low reaction temperature is one reason for the excellent stability of fcc NCs in aqueous-phase FTS reactions. In another aspect, as demonstrated in previous work,^{59,70} the epitaxial deposited Ru layers on the fcc Pt core are “locked”, retaining the fcc crystal structure in the formation of fcc Ru shell because of the favorable interfacial adhesion. We note that the presence of Pt core may influence the activity of Ru shell via the so-called ligand effect and strain effect. To explore the potential influence, we calculated CO adsorption and dissociation on two and four Ru epitaxial layers on Pt(111) (Tables S2–5). For thinner (two) Ru layers on Pt(111), CO adsorption was weakened by 0.17 eV, and the CO dissociation barrier increased by 0.02 eV. For the thicker (four) Ru layer on Pt(111) whose ligand effect was reduced, CO adsorption was weakened by 0.04 eV, and the CO dissociation barrier decreased by 0.1 eV. Since the Ru shell is typically thicker than four layers (~ 1 nm), the influence of the Pt core on activity of the Ru shell was expected to be modest. In other words, the superior activity of fcc NCs comes intrinsically from the Ru shell.

Most importantly, the super mass specific activity of fcc NCs is achieved not by decrease of the particle size but by the increase of the site density, a fact of that becomes possible by taking advantage of the distinct crystal structure of fcc Ru. As a result, the catalysts with super mass-specific activity can be maintained in a relative large size (6.8 nm) and are thermodynamically more resistant toward sintering, oxidation, and disintegration, etc.

CONCLUSION

For CO dissociation, density functional theory calculations show that there are a number of open facets with modest barriers available on fcc Ru but only few step edges with a lower barrier on hcp Ru. Accordingly, fcc Ru may have a higher specific activity. Guided by theoretical calculations, water-dispersible fcc Ru NCs catalysts with abundant open facets were synthesized. The fcc NCs Ru catalysts synthesized are highly active for aqueous-phase FTS even in 393–433 K. The catalysts with average size of 6.8 nm show an unprecedented mass-specific activity, which is about three times larger than the previous best hcp Ru catalyst with a smaller size of 1.9 nm and a higher specific surface area. The origin is identified from the formation of 2 orders of magnitude higher density of the active sites, overcompensating its higher apparent barrier, as predicted by theory.

The present investigation presents a strategy to a rational design of catalysts for high mass-specific activity by exploiting the crystal phases with different site abundance and intrinsic activity. Since the different crystal phases of catalysts could be controlled by the temperature, pressure, particle size, and metal–support interaction, and prepared even by dedicated synthesized methods, utilization of the crystal phases might open a new dimension of the rational design of catalysts toward a higher mass-specific activity. The presence of denser active

sites allows the synthesis of the catalysts for a higher mass-specific activity without necessary decrease of the particle size, a fact of that can significantly improve the stability of catalysts.

■ COMPUTATIONAL METHODOLOGY

All of the density functional theory (DFT) calculations were performed by using projector augmented wave (PAW)⁸⁰ potentials and the Perdew–Burke–Ernzerhof (PBE) functional⁸¹ as implemented in the Vienna ab initio simulation package (VASP).^{82,83} The plane wave cutoff energy was set at 400 eV. The $p(1 \times 1)$ slab models used here have an atomic thickness of at least 19.5 Å and are separated by a vacuum of 15 Å for the accurate surface energies calculations. All of the atoms are fully relaxed for the surface energy calculations. A Monkhorst–Pack⁸⁴ k -point sampling of $12 \times 12 \times 1$ is adopted for the hcp Ru (0001) surface and is scaled proportionally for other surface unit cells.

We have used $p(2 \times 2)$ slab models for CO activation on all of the facets exposed on the morphologies of hcp and fcc Ru. All of the facets were simulated by four equivalent (111) layers (except fcc Ru (100) surface with five layers) slab. Neighboring slabs were separated by a vacuum of 15 Å to avoid the interactions between them. The density of k -points were kept at $\sim 0.04 \text{ \AA}^{-1}$. All the adsorbates and the topmost two equivalent (111) layers were relaxed. The improved force reversed method⁸⁵ was used to locate the transition states (TS), and the force tolerance was 0.03 eV/Å. Some of the TS are verified by the climbing-image nudged elastic band (CI-NEB) methods.^{86,87} The located TS for CO dissociation were confirmed by frequency analysis.

The surface energy is calculated as $E_{\text{sur}} = (E_{\text{slab}} - NE_{\text{bulk}})/2A$, where E_{slab} and E_{bulk} are the total energy of the slab and one bulk Ru atom, respectively, N is the number of Ru atoms in the slab, and A is the surface area. CO activation barrier (E_a) is calculated as the energy difference between the transition state and initial state. The reaction energy (ΔE) is the energy difference between the total energies of final state and initial state. We chose the separate most stable adsorbed fragments on the surface as the initial and final states. The determined equilibrium lattice constants based on DFT calculations for bulk hcp and fcc Ru are $a = b = 2.728 \text{ \AA}$, $c = 4.297 \text{ \AA}$, and $a = b = c = 3.818 \text{ \AA}$, respectively.

The vibration frequency factor A_{vib} for CO dissociation was calculated via the following equation based on the transition-state theory:

$$A_{\text{vib}} = \frac{k_{\text{B}}T}{h} \frac{Q_{\text{TS}}}{Q_{\text{CO}}}, \quad Q_{\text{TS}(\text{CO})} = \prod_i 1/(1 - \exp[-h\nu_i/k_{\text{B}}T])$$

Q_{TS} and Q_{CO} are the partition functions of CO dissociation at the transition state and adsorption state within the ideal gas rigid-rotor harmonic oscillator approximation. Vibrational frequencies were calculated by DFT.

■ EXPERIMENTAL PROCEDURES

Chemicals. Syngas (CO 32%, H₂ 64%, Ar 4%) was purchased from Beijing AP BAIF Gases Industry Co., Ltd. H₂ (99.999%), RuCl₃· x H₂O (A.R., Shengyang Institute of Nonferrous Metal), K₂PtCl₄ (A.R., Shengyang Institute of Nonferrous Metal), ruthenium(III) 2,4-pentanedionate (Ru(acac)₃, Alfa Aesar), benzyl alcohol (A.R.), poly(*N*-vinyl-2-pyrrolidone) (PVP, MW \sim 29000, Sigma-Aldrich), formaldehyde solution (HCHO, 40%, A.R.), hydrochloride acid (HCl, A.R.), acetone (A.R.), cyclohexane (HPLC grade), naphthane (AR grade), and other chemicals were commercially available and used without further purification.

Catalyst Synthesis. The hydrothermal synthesis of fcc NCs was carried out in 25 mL Teflon-lined containers sealed in stainless steel autoclaves. In the synthesis, 0.024 mmol of K₂PtCl₄, 0.216 mmol of RuCl₃· x H₂O, 100 mg of PVP, 0.1 mL of HCHO solution, and 0.062 mL of 1 M HCl solution were dissolved in ultrapure water (Millipore, 18.2 MΩ), diluted to 15 mL, added into the container, and sealed in the autoclave. The autoclave was then transferred into an oven kept at 433 K and taken out after 8 h. After the autoclave was cooled to room

temperature, 45 mL of acetone was added, and the nanocrystals were collected by centrifugation at 10000 rpm for 10 min.

hcp NCs (6.8 nm) were synthesized with a solvothermal method in 25 mL Teflon-lined containers sealed in stainless steel autoclaves. Ru(acac)₃ (0.24 mmol) and PVP (100 mg) were dissolved in 10 mL of benzyl alcohol. The solvothermal reaction was kept at 423 K for 24 h. After the autoclave was cooled to room temperature, 40 mL of acetone was added, and the nanocrystals were collected by centrifugation at 10000 rpm for 10 min.

hcp NCs (1.9 nm) were synthesized using the same method as that of Xiao et al.¹⁸ In a typical experiment, 0.2 mmol of RuCl₃· x H₂O and 0.88 g of PVP (8 mmol, PVP/Ru = 40:1 mol ratio) were dissolved in 40 mL of deionized water. The solution was then placed in a 100 mL stainless steel autoclave and was reduced under 2.0 MPa H₂ at 423 K for 2 h with 800 rpm stirring. The reduced hcp NCs (1.9 nm) was used for the AFTS directly.

TEM Characterization. For TEM, the fcc NCs aqueous solution was appropriately diluted with acetone and dispersed by ultrasonication for 15 min, then one drop of solution was placed on a copper grid coated by carbon film. The TEM measurements were carried out on TECNAI F30 and JEM-2100 transmission electron microscope operating at 300 kV and 200 kV.

Aberation corrected STEM imaging and EELS mapping were performed on a Nion UltraSTEM-100, operated at 100 kV. The elemental mapping of Pt and Ru via STEM-EELS spectrum imaging was acquired using the Pt O-edge at 52 eV and Ru N-edge at 43 eV, respectively. Due to the partial overlapping of the Pt O-edge and Ru N-edge, multiple linear least-squares (MLLS) fitting of the as-acquired low-loss spectrum imaging was performed using reference spectra from metallic Pt and metallic Ru. The fitting residuals were carefully examined to make sure that the residuals are in the noise level. STEM-ADF image simulation was performed using QSTEM from <http://qstem.org/>.

XRD Characterization. The XRD measurements were carried out on an X pert pro diffractometer (Philips, Netherland) using Cu K α radiation ($\lambda = 1.5406 \text{ \AA}$) with a scan speed of 2° min^{-1} . The contribution of the K α_2 line was subtracted.

XAFS Characterization. The XAFS spectra of Ru K edge (22117 eV) for fcc NCs were collected at the BL14W1 beamline of the Shanghai Synchrotron Radiation Facility (SSRF) operated at 3.5 GeV under “top-up” mode with a constant current of 240 mA under fluorescence mode. Pt L3 edge (11564 eV) data were collected at the 1W1B beamline of the Beijing Synchrotron Radiation Facility (BSRF) under fluorescence mode. The focused beam was tuned by the Si(111) double-crystal monochromators for Pt L3 edge, while the unfocused beam was tuned by the Si(311) double-crystal monochromators for Ru K edge. The energies were calibrated according to the absorption edge of pure Pt and Ru foils. For the XAFS measurements on Pt L3 edge and the Ru K edge, about 0.05 mol·L⁻¹ aqueous solution of as-prepared fcc NCs was sealed in 2 mm liquid cell with Kapton film windows.

All of the collected spectra were processed and analyzed using Athena and Artemis code within the Iffedit package.⁸⁸ For the X-ray absorption near edge structure (XANES) part, the experimental absorption coefficients as a function of energies were processed by background subtraction and normalization procedures, and reported as “normalized intensity”. Besides Pt and Ru foils, the PtO₂ and RuO₂ bulk materials were also used as references. For the extended X-ray absorption fine structure (EXAFS) part, the Fourier transform (FT) data in R space were analyzed by applying fcc Pt and fcc Ru models for Pt–Pt/Pt–Ru shell and Ru–Ru/Ru–Pt shell in fcc NCs, respectively. The passive electron factors, S_0^2 , were determined by fitting the experimental Pt and Ru foils data and fixing the Pt–Pt and Ru–Ru coordination number (CN) to be 12 and 6 + 6, respectively, and then fixed for further analysis of the measured samples. The parameters describing the electronic properties (e.g., correction to the photoelectron energy origin, E_0) and local structure environment including CN, bond distance (R), and Debye–Waller factor (σ^2) around the absorbing atoms were allowed to vary during the fitting process. The fitted ranges for k and R spaces (k^2 weighted) were selected to be $k =$

2.8–15.1 Å⁻¹ (Pt–Pt/Pt–Ru) or 3.4–14.0 Å⁻¹ (Ru–Ru/Ru–Pt) and R = 1.9–3.6 (Pt–Pt/Pt–Ru), or 1.8–3.5 Å (Ru–Ru/Ru–Pt), respectively. More information can be found in the [Appendix](#).

■ ASSOCIATED CONTENT

📄 Supporting Information

The Supporting Information is available free of charge on the ACS Publications website at DOI: [10.1021/jacs.6b10375](https://doi.org/10.1021/jacs.6b10375).

Detailed Information about DFT calculations, XAFS spectra of catalysts, more ADF images of catalysts, and detailed product distributions ([PDF](#))

Proposed fcc NCs model ([AVI](#))

■ AUTHOR INFORMATION

Corresponding Authors

*wqli70@ustc.edu.cn

*ywzhang@pku.edu.cn

*dma@pku.edu.cn

ORCID

Wei-Xue Li: [0000-0002-5043-3088](https://orcid.org/0000-0002-5043-3088)

Ding Ma: [0000-0002-3341-2998](https://orcid.org/0000-0002-3341-2998)

Author Contributions

⊗W.-Z.L., J.-X.L., and J.G. contributed equally.

Notes

The authors declare no competing financial interest.

■ ACKNOWLEDGMENTS

This work received financial support from the National Natural Science Foundation of China (Grant Nos. 21225315, 91645202, 21473003, 21273224, 21573005, 21621061, and 21271011), Chinese Academy of Sciences, the National Key Research and Development Program of China (Grant Nos. 2013CB834603, 2013CB933100, 2016YFB0701100), Strategic Priority Research Program of the Chinese Academy of Sciences (XDA090301001, XDB17010200), and the Beijing Natural Science Foundation (Grant No. 2162019). The electron microscopy work was supported by the U.S. Department of Energy, Office of Science, Basic Energy Science, Materials Sciences and Engineering Division, and through a user project at ORNL's Center for Nanophase Materials Sciences (CNMS), which is a DOE Office of Science User Facility. The EXAFS experiments were conducted in SSRF and BSRF. We acknowledge Prof. M. Chen's help in SIMS experiments and Dr. Bryan Goldsmith for reading the manuscript carefully.

■ REFERENCES

- (1) Torres Galvis, H. M.; Bitter, J. H.; Khare, C. B.; Ruitenbeek, M.; Dugulan, A. I.; de Jong, K. P. *Science* **2012**, *335*, 835–838.
- (2) Vannice, M. J. *Catal.* **1975**, *37*, 449–461.
- (3) Iglesia, E. *Appl. Catal., A* **1997**, *161*, 59–78.
- (4) Zhang, Q.; Kang, J.; Wang, Y. *ChemCatChem* **2010**, *2*, 1030–1058.
- (5) Schulz, H. *Appl. Catal., A* **1999**, *186*, 3–12.
- (6) Sartipi, S.; Parashar, K.; Makkee, M.; Gascon, J.; Kapteijn, F. *Catal. Sci. Technol.* **2013**, *3*, 572–575.
- (7) Vervloet, D.; Kapteijn, F.; Nijenhuis, J.; van Ommen, J. R. *Catal. Sci. Technol.* **2012**, *2*, 1221–1233.
- (8) Bezemer, G. L.; Bitter, J. H.; Kuipers, H. P.; Oosterbeek, H.; Holewijn, J. E.; Xu, X.; Kapteijn, F.; van Dillen, A. J.; de Jong, K. P. *J. Am. Chem. Soc.* **2006**, *128*, 3956–3964.
- (9) Santos, V. P.; Wezendonk, T. A.; Jaén, J. J. D.; Dugulan, A. I.; Nasalevich, M. A.; Islam, H.-U.; Chojecki, A.; Sartipi, S.; Sun, X.; Hakeem, A. A. *Nat. Commun.* **2015**, *6*, 6451.

- (10) Calderone, V. R.; Shiju, N. R.; Curulla-Ferré, D.; Chambrey, S.; Khodakov, A.; Rose, A.; Thiessen, J.; Jess, A.; Rothenberg, G. *Angew. Chem., Int. Ed.* **2013**, *52*, 4397–4401.
- (11) Calderone, V. R.; Shiju, N. R.; Ferré, D. C.; Rothenberg, G. *Green Chem.* **2011**, *13*, 1950–1959.
- (12) Khodakov, A. Y.; Griboval-Constant, A.; Bechara, R.; Zholobenko, V. L. *J. Catal.* **2002**, *206*, 230–241.
- (13) Khodakov, A. Y.; Chu, W.; Fongarland, P. *ChemInform* **2007**, DOI: [10.1002/chin.200733255](https://doi.org/10.1002/chin.200733255).
- (14) Schweicher, J.; Bundhoo, A.; Kruse, N. *J. Am. Chem. Soc.* **2012**, *134*, 16135–16138.
- (15) Xiang, Y.; Barbosa, R.; Kruse, N. *ACS Catal.* **2014**, *4*, 2792–2800.
- (16) van Steen, E.; Claeys, M.; Dry, M. E.; van de Loosdrecht, J.; Viljoen, E. L.; Visagie, J. L. *J. Phys. Chem. B* **2005**, *109*, 3575–3577.
- (17) Riedel, T.; Claeys, M.; Schulz, H.; Schaub, G.; Nam, S.-S.; Jun, K.-W.; Choi, M.-J.; Kishan, G.; Lee, K.-W. *Appl. Catal., A* **1999**, *186*, 201–213.
- (18) Xiao, C. x.; Cai, Z. p.; Wang, T.; Kou, Y.; Yan, N. *Angew. Chem.* **2008**, *120*, 758–761.
- (19) Quek, X. Y.; Guan, Y.; van Santen, R. A.; Hensen, E. J. *ChemCatChem* **2011**, *3*, 1735–1738.
- (20) Lan, G.; Yao, Y.; Zhang, X.; Guo, M.; Tang, H.; Li, Y.; Yang, Q. *Catal. Sci. Technol.* **2016**, *6*, 2181–2187.
- (21) Van Santen, R. A. *Acc. Chem. Res.* **2009**, *42*, 57–66.
- (22) Den Breejen, J.; Radstake, P.; Bezemer, G.; Bitter, J.; Froseth, V.; Holmen, A.; Jong, K. P. *J. Am. Chem. Soc.* **2009**, *131*, 7197.
- (23) Valden, M. *Science* **1998**, *281*, 1647–1650.
- (24) Narayanan, R.; El-Sayed, M. A. *J. Am. Chem. Soc.* **2003**, *125*, 8340–8347.
- (25) Narayanan, R.; El-Sayed, M. A. *J. Phys. Chem. B* **2005**, *109*, 12663–12676.
- (26) Ouyang, R.; Liu, J.-X.; Li, W.-X. *J. Am. Chem. Soc.* **2013**, *135*, 1760–1771.
- (27) Goldsmith, B. R.; Sanderson, E. D.; Ouyang, R.; Li, W.-X. *J. Phys. Chem. C* **2014**, *118*, 9588–9597.
- (28) Munnik, P.; Velthoen, M. E.; De Jongh, P. E.; De Jong, K. P.; Gommers, C. J. *Angew. Chem., Int. Ed.* **2014**, *53*, 9493–9497.
- (29) Munnik, P.; de Jongh, P. E.; de Jong, K. P. *J. Am. Chem. Soc.* **2014**, *136*, 7333–7340.
- (30) Da Silva, A. L.; Den Breejen, J. P.; Mattos, L. V.; Bitter, J. H.; De Jong, K. P.; Noronha, F. B. *J. Catal.* **2014**, *318*, 67–74.
- (31) Carballo, J. M. G.; Yang, J.; Holmen, A.; García-Rodríguez, S.; Rojas, S.; Ojeda, M.; Fierro, J. L. G. *J. Catal.* **2011**, *284*, 102–108.
- (32) Kellner, C. S.; Bell, A. T. *J. Catal.* **1982**, *75*, 251–261.
- (33) Behrens, M.; Studt, F.; Kasatkin, I.; Kühl, S.; Hävecker, M.; Abild-Pedersen, F.; Zander, S.; Girgsdies, F.; Kurr, P.; Knief, B.-L. *Science* **2012**, *336*, 893–897.
- (34) Lopez, N.; Nørskov, J. K. *J. Am. Chem. Soc.* **2002**, *124*, 11262–11263.
- (35) Honkala, K.; Hellman, A.; Remediakis, I. N.; Logadottir, A.; Carlsson, A.; Dahl, S.; Christensen, C. H.; Nørskov, J. K. *Science* **2005**, *307*, 555–558.
- (36) Callegari, A.; Tonti, D.; Chergui, M. *Nano Lett.* **2003**, *3*, 1565–1568.
- (37) Jana, N. R.; Gearheart, L.; Murphy, C. J. *Adv. Mater.* **2001**, *13*, 1389.
- (38) Sun, Y.; Xia, Y. *Science* **2002**, *298*, 2176–2179.
- (39) Zhou, K.; Li, Y. *Angew. Chem., Int. Ed.* **2012**, *51*, 602–613.
- (40) Wang, C.; Daimon, H.; Lee, Y.; Kim, J.; Sun, S. *J. Am. Chem. Soc.* **2007**, *129*, 6974–6975.
- (41) Lara, P.; Conejero, S.; Poteau, R.; Philippot, K.; Chaudret, B.; Rivada-Wheelaghan, O. *Angew. Chem., Int. Ed.* **2011**, *50*, 12080–12084.
- (42) Ducreux, O.; Lynch, J.; Rebours, B.; Roy, M.; Chaumette, P. *Stud. Surf. Sci. Catal.* **1998**, *119*, 125–130.
- (43) Ducreux, O.; Rebours, B.; Lynch, J.; Roy-Auberger, M.; Bazin, D. *Oil Gas Sci. Technol.* **2009**, *64*, 49–62.

- (44) Sadeqzadeh, M.; Karaca, H.; Safonova, O.; Fongarland, P.; Chambrey, S.; Roussel, P.; Griboval-Constant, A.; Lacroix, M.; Curulla-Ferré, D.; Luck, F. *Catal. Today* **2011**, *164*, 62–67.
- (45) de la Peña O'Shea, V. A.; Homs, N.; Fierro, J. L. G.; Ramírez de la Piscina, P. *Catal. Today* **2006**, *114*, 422–427.
- (46) Enache, D. I.; Rebours, B.; Roy-Auberger, M.; Revel, R. *J. Catal.* **2002**, *205*, 346–353.
- (47) Gnanamani, M. K.; Jacobs, G.; Shafer, W. D.; Davis, B. H. *Catal. Today* **2013**, *215*, 13–17.
- (48) Liu, J.-X.; Su, H.-Y.; Sun, D.-P.; Zhang, B.-Y.; Li, W.-X. *J. Am. Chem. Soc.* **2013**, *135*, 16284–16287.
- (49) Liu, J. X.; Li, W. X. *WIREs Comput. Mol. Sci.* **2016**, *6*, 571–583.
- (50) Mou, X.; Zhang, B.; Li, Y.; Yao, L.; Wei, X.; Su, D. S.; Shen, W. *Angew. Chem., Int. Ed.* **2012**, *51*, 2989–2993.
- (51) Guo, Y.; Liu, X.; Azmat, M. U.; Xu, W.; Ren, J.; Wang, Y.; Lu, G. *Int. J. Hydrogen Energy* **2012**, *37*, 227–234.
- (52) Dong, W.; Liu, J.; Zhu, H.; Ding, Y.; Pei, Y.; Liu, J.; Du, H.; Jiang, M.; Liu, T.; Su, H.; Li, W. *J. Phys. Chem. C* **2014**, *118*, 19114–19122.
- (53) Fan, Z.; Zhang, H. *Chem. Soc. Rev.* **2016**, *45*, 63–82.
- (54) Liu, J.-X.; Zhang, B.-Y.; Chen, P.-P.; Su, H.-Y.; Li, W.-X. *J. Phys. Chem. C* **2016**, *120*, 24895–24903.
- (55) Pei, Y.-P.; Liu, J.-X.; Zhao, Y.-H.; Ding, Y.-J.; Liu, T.; Dong, W.-D.; Zhu, H.-J.; Su, H.-Y.; Yan, L.; Li, J.-L.; Li, W.-X. *ACS Catal.* **2015**, *5*, 3620–3624.
- (56) Zhong, L.; Yu, F.; An, Y.; Zhao, Y.; Sun, Y.; Li, Z.; Lin, T.; Lin, Y.; Qi, X.; Dai, Y. *Nature* **2016**, *538*, 84–87.
- (57) Joo, S. H.; Park, J. Y.; Renzas, J. R.; Butcher, D. R.; Huang, W.; Somorjai, G. A. *Nano Lett.* **2010**, *10*, 2709–2713.
- (58) Kusada, K.; Kobayashi, H.; Yamamoto, T.; Matsumura, S.; Sumi, N.; Sato, K.; Nagaoka, K.; Kubota, Y.; Kitagawa, H. *J. Am. Chem. Soc.* **2013**, *135*, 5493–5496.
- (59) Gu, J.; Guo, Y.; Jiang, Y.-Y.; Zhu, W.; Xu, Y.-S.; Zhao, Z.-Q.; Liu, J.-X.; Li, W.-X.; Jin, C.-H.; Yan, C.-H. *J. Phys. Chem. C* **2015**, *119*, 17697–17706.
- (60) Abo-Hamed, E. K.; Pennycook, T.; Vaynzof, Y.; Toprakcioglu, C.; Koutsoubas, A.; Scherman, O. A. *Small* **2014**, *10*, 3145–3152.
- (61) Ma, H.; Na, C. *ACS Catal.* **2015**, *5*, 1726–1735.
- (62) Ye, H.; Wang, Q.; Catalano, M.; Lu, N.; Vermeulen, J.; Kim, M. J.; Liu, Y.; Sun, Y.; Xia, X. *Nano Lett.* **2016**, *16*, 2812–2817.
- (63) AlYami, N. M.; LaGrow, A. P.; Joya, K. S.; Hwang, J.; Katsiev, K.; Anjum, D. H.; Losovyj, Y.; Sinatra, L.; Kim, J. Y.; Bakr, O. M. *Phys. Chem. Chem. Phys.* **2016**, *18*, 16169–16178.
- (64) Yao, Y.; He, D. S.; Lin, Y.; Feng, X.; Wang, X.; Yin, P.; Hong, X.; Zhou, G.; Wu, Y.; Li, Y. *Angew. Chem.* **2016**, *128*, 5591–5595.
- (65) Zhao, M.; Figueroa-Cosme, L.; Elnabawy, A. O.; Vara, M.; Yang, X.; Roling, L. T.; Chi, M.; Mavrikakis, M.; Xia, Y. *Nano Lett.* **2016**, *16*, 5310–5317.
- (66) Shetty, S.; Jansen, A. P. J.; van Santen, R. A. *J. Am. Chem. Soc.* **2009**, *131*, 12874–12875.
- (67) Shetty, S.; van Santen, R. A. *Catal. Today* **2011**, *171*, 168–173.
- (68) Shetty, S.; van Santen, R. A. *Top. Catal.* **2010**, *53*, 969–975.
- (69) Wang, H.; Zhou, W.; Liu, J.-X.; Si, R.; Sun, G.; Zhong, M.-Q.; Su, H.-Y.; Zhao, H.-B.; Rodriguez, J. A.; Pennycook, S. J.; Idrobo, J.-C.; Li, W.-X.; Kou, Y.; Ma, D. *J. Am. Chem. Soc.* **2013**, *135*, 4149–4158.
- (70) Alayoglu, S.; Zavalij, P.; Eichhorn, B.; Wang, Q.; Frenkel, A. I.; Chupas, P. *ACS Nano* **2009**, *3*, 3127–3137.
- (71) Yin, A.-X.; Min, X.-Q.; Zhang, Y.-W.; Yan, C.-H. *J. Am. Chem. Soc.* **2011**, *133*, 3816–3819.
- (72) Yin, A.-X.; Min, X.-Q.; Zhu, W.; Wu, H.-S.; Zhang, Y.-W.; Yan, C.-H. *Chem. Commun.* **2012**, *48*, 543–545.
- (73) Wang, C.; Zhao, H.; Wang, H.; Liu, L.; Xiao, C.; Ma, D. *Catal. Today* **2012**, *183*, 143–153.
- (74) Quek, X.-Y.; Pestman, R.; van Santen, R. A.; Hensen, E. J. *Catal. Sci. Technol.* **2014**, *4*, 3510–3523.
- (75) Turner, M. L.; Marsih, N.; Mann, B. E.; Quyoun, R.; Long, H. C.; Maitlis, P. M. *J. Am. Chem. Soc.* **2002**, *124*, 10456–10472.
- (76) Claeys, M.; van Steen, E. *Catal. Today* **2002**, *71*, 419–427.
- (77) Shi, D.; Faria, J.; Pham, T. N.; Resasco, D. E. *ACS Catal.* **2014**, *4*, 1944–1952.
- (78) Cheng, J.; Hu, P.; Ellis, P.; French, S.; Kelly, G.; Lok, C. M. *Top. Catal.* **2010**, *53*, 326–337.
- (79) Cheng, J.; Hu, P.; Ellis, P.; French, S.; Kelly, G.; Lok, C. M. *J. Phys. Chem. C* **2009**, *113*, 8858–8863.
- (80) Blöchl, P. E. *Phys. Rev. B: Condens. Matter Mater. Phys.* **1994**, *50*, 17953.
- (81) Perdew, J. P.; Burke, K.; Ernzerhof, M. *Phys. Rev. Lett.* **1996**, *77*, 3865–3868.
- (82) Kresse, G.; Hafner, J. *Phys. Rev. B: Condens. Matter Mater. Phys.* **1993**, *47*, 558.
- (83) Kresse, G.; Furthmüller, J. *Phys. Rev. B: Condens. Matter Mater. Phys.* **1996**, *54*, 11169.
- (84) Monkhorst, H. J.; Pack, J. D. *Phys. Rev. B* **1976**, *13*, 5188–5192.
- (85) Sun, K.; Zhao, Y.; Su, H. Y.; Li, W. X. *Theor. Chem. Acc.* **2012**, *131*, 1–10.
- (86) Henkelman, G.; Uberuaga, B. P.; Jónsson, H. *J. Chem. Phys.* **2000**, *113*, 9901.
- (87) Henkelman, G.; Jónsson, H. *J. Chem. Phys.* **2000**, *113*, 9978.
- (88) Ravel, B.; Newville, M. *J. Synchrotron Radiat.* **2005**, *12*, 537–541.